CHEMISTRY OF MATERIALS

Article

pubs.acs.org/cm

From Linear Molecular Chains to Extended Polycyclic Networks: Polymerization of Dicyanoacetylene

Huiyang Gou,[*,†,‡,○] Li Zhu,[†,○] Haw-Tyng Huang,[■,¶] Arani Biswas,[§,■] Derek W. Keefer,[§,■] Brian L. Chaloux,[∥,◆] Clemens Prescher,[⊥] Liuxiang Yang,[†,‡] Duck Young Kim,[†,‡] Matthew D. Ward,[†] Jordan Lerach,[■] Shengnan Wang,[#] Artem R. Oganov,[#,▽] Albert Epshteyn,[∥] John V. Badding,[§,■,¶,□] and Timothy A. Strobel[*,†]

[†]Geophysical Laboratory, Carnegie Institution of Washington, Washington, DC 20015, United States

[‡]Center for High Pressure Science and Technology Advanced Research, Beijing 100094, China

[§]Department of Chemistry, The Pennsylvania State University, University Park, Pennsylvania 16802, United States

[■]Materials Research Institute, The Pennsylvania State University, University Park, Pennsylvania 16802, United States

[¶]Department of Materials Science and Engineering, The Pennsylvania State University, University Park, Pennsylvania 16802, United States

[□]Department of Physics, The Pennsylvania State University, University Park, Pennsylvania 16802, United States

[∥]Naval Research Laboratory, 4555 Overlook Avenue, SW, Washington, DC 20375, United States

[⊥]Center for Advanced Radiation Sources, University of Chicago, Argonne, Illinois 60437, United States

[#]Department of Geosciences, Center for Materials by Design, and Institute for Advanced Computational Science, State University of New York, Stony Brook, New York 11794-2100, United States

[▽]Skolkovo Institute of Science and Technology, Skolkovo Innovation Center, 3 Nobel Street, Moscow 143026, Russia

Supporting Information

ABSTRACT: Dicyanoacetylene (C_4N_2) is an unusual energetic molecule with alternating triple and single bonds (think miniature, nitrogen-capped carbyne), which represents an interesting starting point for the transformation into extended carbon−nitrogen solids. While pressure-induced polymerization has been documented for a wide variety of related molecular solids, precise mechanistic details of reaction pathways are often poorly understood and the characterization of recovered products is typically incomplete. Here, we study the high-pressure behavior of C_4N_2 and demonstrate polymerization into a disordered carbon−nitrogen network that is recoverable to ambient conditions. The reaction proceeds via activation of linear molecules into buckled molecular chains, which spontaneously assemble into a polycyclic network that lacks long-range order. The recovered product was characterized using a variety of optical spectroscopies, X-ray methods, and theoretical simulations and is described as a predominately sp^2 network comprising "pyrrolic" and "pyridinic" rings with an overall tendency toward a two-dimensional structure. This understanding offers valuable mechanistic insights into design guidelines for next-generation carbon nitride materials with unique structures and compositions.

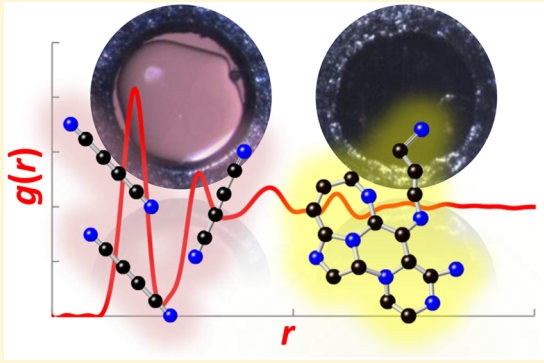

INTRODUCTION

Carbon nitride materials have attracted continuous attention in research over past decades as indicated by extensive efforts from both theory[1,2] and experiments.[3−19] Sustained interest in nitrogen-bearing, carbon-rich materials stems from their multiple functionalities and diverse applications.[1−19] For example, cubic carbon nitride (c-C_3N_4) is predicted to have hardness comparable to diamond,[1,2] whereas graphitic carbon nitride (g-C_3N_4) has been demonstrated to act as a photocatalyst for various redox reactions.[4−19] Furthermore, nitrogen-doped carbon materials often exhibit excellent properties as compared with their pure carbon counterparts, e.g., conductivity, basicity, oxidation stability, and catalytic activity, although these properties are highly dependent on the amount of nitrogen incorporated within the structure.[4−19] When long-range order within carbon nitride materials is lacking, disordered structures containing sp^2 and sp^3 bonding may still exhibit outstanding mechanical properties,[20−26] which is

Received: April 8, 2017
Revised: June 23, 2017
Published: June 26, 2017

DOI: 10.1021/acs.chemmater.7b01446
Chem. Mater. 2017, 29, 6706−6718

fundamentally important for the realization of three-dimensional, crystalline carbon nitride solids.

Previous attempts to produce novel CN solids have largely revolved around varying deposition methods to manipulate particle size and texture, together with control of nitrogen content.[10−17] Nevertheless, adventitious hydrogen incorporation within these materials limits the development of structure−property relationships for precise stoichiometries and diverse CN building blocks.[27−32] High-energy molecules can provide an alternative path toward the formation of unique structures, and high-pressure chemistry may be a viable approach to obtain novel extended CN networks with predetermined architectures.[33] Studies of the polymerization reactions of cyanogen,[34] cyanoacetylene,[35] tetracyanoethylene,[36] phosphorus tricyanide,[37] and acetonitrile[38] under pressure have helped to clarify the influences of starting materials and reaction conditions for the synthesis of new CN materials.

Dicyanoacetylene (C_4N_2) is a linear molecule with alternating triple and single bonds (N≡C−C≡C−C≡N).[39] The standard enthalpy of formation of C_4N_2 is 500 kJ/mol,[40] leading to a flame temperature of over 5000 K.[41] Thus, C_4N_2 represents an interesting, high-energy starting point to access novel extended CN networks. From the low-pressure side, people have examined C_4N_2 and found reactions with benzene to produce aromatic hydrocarbons via the Diels−Alder reaction,[42] in addition to explosive decomposition into dinitrogen and graphite. Chien and Carlini synthesized poly(dicyanoacetylene) via anionic polymerization of C_4N_2 with *n*-butyllithium in THF, producing a linear polymer that cyclizes into a ladder polymer upon heating at 400 °C.[43] Interestingly, the physiochemical behavior of C_4N_2 is also of astrophysical importance due to its presence in Titan's north polar stratosphere,[44−47] as detected by infrared spectroscopy. However, the interpretation of Raman and IR spectra is challenging, especially with regard to conflicting assignments for C≡N and C≡C stretching frequencies.[48−54] Inconsistencies between spectroscopic assignments for C_4N_2 may arise from difficulties associated with sample preparation and handling due to its inherent instability and high reactivity; although it is of great importance for the understanding of intrinsic properties and conclusions regarding its detection.

To our knowledge, C_4N_2 has not yet been examined under high-pressure conditions, which is of great interest from the perspective of novel carbon nitride materials and fundamental chemical transformations. The large fraction of unsaturated bonds suggests potential for pressure-induced ring-forming reactions, as has been documented for a large number of other nitrile- and alkyne-based systems.[34−38] In addition, C_4N_2 represents an interesting C:N stoichiometry to access extended networks with nitrogen content intermediate between typical deposition-based syntheses (nitrogen doping within a carbon framework) and precursor-based systems such as graphitic C_3N_4. Moreover, high-pressure behavior can help to understand the nature of chemical bonding, reaction mechanisms, atomic structure, and local environments of reaction products, which will advance the general understanding of carbon nitride materials.

Here, we study the high-pressure behavior of linear dicyanoacetylene (C_4N_2) up to 10 GPa in diamond anvil cells. We first resolve the standing controversy regarding assignments of Raman and IR spectra, aided by first-principles phonon spectrum calculations. We next uncover a pressure-induced reaction process whereby discrete linear molecules polymerize into a disordered extended network without significant change to the bulk composition. This novel, amorphous material is fully recoverable to ambient conditions, and its local structure, composition, and chemical bonding were established using a variety of optical and X-ray scattering methods. The reaction mechanism was rationalized using molecular dynamics simulations. The present results provide a framework to further the understanding of the local mechanism of polymerization and offer valuable mechanistic insights into design guidelines for the next-generation carbon nitride materials.

METHODS

Synthesis. C_4N_2 was prepared according to literature procedures.[55] All reactions were performed under an inert atmosphere of either nitrogen or argon. Diethyl ether was dried and deoxygenated over sodium−benzophenone ketyl prior to use. Sulfolane was purified by reaction with $KMnO_4$ to remove alkene impurities, dried over KOH, and vacuum distilled prior to use.

*Acetylene Dicarboxamide (**1**).* A 100 mL aliquot of NH_3 (4.8 mol) was condensed into a Schlenk flask and chilled to −78 °C. Separately, 13.41 g (94.36 mmol) of dimethyl acetylenedicarboxylate (Sigma-Aldrich, 99%) was dissolved in 100 mL of anhydrous diethyl ether (Et_2O) and transferred dropwise to the chilled flask containing NH_3; the reaction mixture quickly developed a red coloration. The reaction mixture was warmed to −45 °C and stirred for 16 h at this temperature. Residual NH_3 was boiled off at ambient temperature, and the remainder was evaporated to dryness under vacuum, yielding a crude, orange product that was subsequently washed with cold ethanol. The resulting beige powder was recrystallized from 150 mL of boiling ethanol at −20 °C, yielding 8.27 g (78% yield) of white, crystalline solid after filtering and drying the powder under vacuum.

*Dicyanoacetylene (**2**).* A 125 mL aliquot of anhydrous sulfolane was added to a Schlenk flask equipped with a solids addition funnel and a secondary (detachable) vacuum trap. Using a mortar and pestle, 1.960 g (17.49 mmol) of acetylene dicarboxamide (**1**) was ground with 15.456 g (54.06 mmol) of P_2O_5 until homogeneous. Solids were added to the addition funnel, the apparatus was evacuated, the trap was chilled to −196 °C, and the sulfolane was heated to 110 °C with vigorous stirring. Solids were added slowly to the reaction mixture, which changed from colorless to yellow to red over time. After bubbling had ceased (∼3 h), the trap containing the crude product was removed and transferred to an argon-filled glovebox, and liquid was pipetted into a small H-tube after melting. The liquid was frozen with LN_2; a static vacuum of 50 mTorr was applied on the assembly. The dewar was transferred to the empty arm of the H-tube, and the product was sublimed by warming the arm. The volatile, pale beige (almost colorless) liquid product was weighed within the glovebox at 0.794 g (60% yield). The product was stored at −35 °C under argon to prevent decomposition.

Poly-C_4N_2. Liquid dicyanoacetylene (**2**; ∼1 μL) was loaded into a ∼150−210 μm diameter hole in a Re gasket using a clean microsyringe. Before sample loading, Re gaskets were preindented to a thickness of 60−80 μm and mounted on 300−500 μm anvil culets of symmetric diamond anvil cells (DAC). Pressure was determined by measurement of fluorescence from a ruby standard placed inside the gasket hole.[56] To avoid any possible contamination of the highly reactive C_4N_2, a pressure medium was not used in the runs, but the molecular crystals are very soft and the influence of deviatoric stresses is expected to be small. All sample loadings were conducted in an inert Ar gas atmosphere glovebox with oxygen and moisture concentrations of less than 1 ppm. All samples were sealed to a starting pressure of ∼0.1 GPa within the inert Ar atmosphere before removing from the glovebox.

Raman Spectroscopy. A system based around a Princeton Instruments spectrograph SP2750 (Trenton, NJ, USA) with a 750 mm focal length was used for the Raman spectra collections. A 532 nm

DOI: 10.1021/acs.chemmater.7b01446
Chem. Mater. 2017, 29, 6706−6718

diode laser was used as an excitation source and was focused through a 20× long working distance objective lens. The laser power was optimized to be ∼1 mW, and a short exposure time of ≤60 s was used to avoid local heating of the sample. Raman light was collected in the backscatter geometry through a 50 μm confocal pinhole, and two narrow-band notch filters (Ondax) were used to allow collection to within ∼10 cm^{-1} from the laser line. Raman light was collected though a 50 μm slit and dispersed off of an 1800 or 300 gr/mm grating onto a liquid nitrogen cooled charge coupled device (CCD) detector providing a spectral resolution of about 2 cm^{-1}. The spectrometer was calibrated using the emission lines of Ne with accuracy < 1 cm^{-1}.

Infrared Spectroscopy. Infrared transmission spectra were collected using a Varian 670-IR spectrometer system (Santa Clara, CA, USA) utilizing a Globar source and KBr mid-/near-IR beam splitter ca. 500−4000 cm^{-1}. Infrared light was focused on and recollected through the sample using reflecting objective lenses. Transmitted light was collimated through a 50 μm pinhole for increased spatial resolution and passed to an HgCdTe detector. IR spectra were recorded at varying pressure. The same diamonds were used to obtain reference spectra after the cell was decompressed and cleaned.

X-ray Diffraction. Powder X-ray diffraction (XRD) measurements up to 13.0 GPa were collected in ∼0.2 GPa pressure increments at the High Pressure Collaborative Access Team (HPCAT), beamline 16-IDB, of the Advanced Photon Source (APS), Argonne National Laboratory (ANL). A monochromatic beam (∼4 × 5 μm^2) with λ = 0.406626 Å was focused on the sample, and data were recorded using a MAR image plate. Diffraction images were processed using the FIT2D data analysis program.[57] Pressure was calibrated by the fluorescence from a Ruby sphere placed inside of the sample chamber.[56] The unit-cell volume and lattice parameters of C_4N_2 were obtained through full profile fitting using the Le Bail[58] method, as implemented in GSAS with EXPGUI.[59,60]

Single-crystal X-ray diffraction studies for C_4N_2 were carried out at the Advanced Photon Source, sector 16-BMD. Monochromatic X-rays (λ = 0.30998 Å) with a beam size of (∼15 × 30 μm^2) were focused on the sample, and room-temperature diffraction was collected using a MAR image plate. The resulting data were processed and indexed using GSE-ADA/RSV.[61] Structure solutions and refinements were completed with the use of the SHELX-14 suite of programs.[62,63] Atom positions were standardized using the program STRUCTURE TIDY.[64,65] Crystallographic images were made using the program CRYSTALMAKER. Further crystallographic details can be found in Supporting Information (SI) Table S1.

The structure factor of recovered amorphous C_4N_2 was measured at the GSECARS 13-IDD beamline, Advanced Photon Source, ANL. The sample was measured with two different incident monochromatic X-ray beam energies: 25 keV (λ = 0.4959 Å) for the low-Q region and 60 keV (λ = 0.2066 Å) for the high-Q region. The beam sizes were 2 × 3 μm^2 and 4 × 5 μm^2, respectively. Diffraction data were collected with a MAR345 image plate, whereby its position was calibrated using a LaB_6 standard. Detector calibration, image integration, and intensity correction for oblique X-ray-to-detector angle were performed using the Dioptas software package.[66] An empty Re gasket with the same thickness as that of the recovered sample was measured as background. The resulting data were stitched together from both measurements. The structure factor, $S(Q)$, and pair distribution function, $g(r)$, were calculated in the Faber−Ziman formalism. Data were collected up to a Q_{max} of 17 $Å^{-1}$. The resulting data were optimized using a Kaplow-type correction[67] with three iterations. A Lorch modification function was used to remove unphysical oscillations in the resulting $g(r)$, which are a result of cutoff effects in the Fourier transformation. The density of the recovered sample was estimated by a method described by Eggert et al.[68]

Scanning Electron Microscopy. The recovered samples within the Re gasket after Raman or infrared spectral measurements were mounted on an Al rod holder for chemical composition mapping and microstructure observations using a field emission scanning electron microscope (FE-SEM; JEOL JSM 6500F) operating at 15 kV and 1.5 nA. Compositional analyses were determined by energy-dispersive X-ray spectroscopy (EDS) using graphite and BN standards.

Transmission Electron Microscopy and Electron Energy Loss Spectroscopy. Transmission electron microscopy (TEM) data collection and analysis were performed using both FEI Tecnai G2 LaB_6 and a FEI Talos F200X transmission electron microscopes. The samples were dispersed on a SiO grid with methanol, and imaging was done under an accelerating voltage of 80 kV for both of the microscopes. Representative EDS data from TEM were collected by a Bruker QUANTAX EDS system attached to the FEI TALOS TEM spectrometer. Electron energy loss (EELS)/energy-filtered TEM measurements were carried out in diffraction mode under 80 kV using the Tecnai G2 LaB_6. Carbon nano-onions (CNOs) were used as a standard for pure 100% sp^2 carbon. Nascent REGAL 250 carbon black was purchased from Cabot Corp. and graphitized at 3573 K for 5 h to form highly crystalline CNOs.

X-ray Photoelectron Spectroscopy. XPS experiments were performed using a Physical Electronics VersaProbe II instrument equipped with a monochromatic Al Kα X-ray source ($h\nu$ = 1,486.7 eV) and a concentric hemispherical analyzer. Charge neutralization was performed using both low-energy electrons (<5 eV) and argon ions. The binding energy axis was calibrated using sputter-cleaned Cu foil (Cu $2p_{3/2}$ = 932.7 eV; Cu $3p_{3/2}$ = 75.1 eV). We assigned the pyridinic-N band in the N 1s spectra to the energy of 398.5 eV. Measurements were made at a takeoff angle of 45° with respect to the sample surface plane. This resulted in a typical sampling depth of 3−6 nm. Quantification was done using locally derived sensitivity factors from a pure poly(vinylpyrrolidone) (PVP) reference sample. A soft surface cleaning was performed using 0.5 kV Ar^+.

TOF-SIMS. Time-of-flight secondary ion mass spectrometry (TOF-SIMS) analysis was performed using a Physical Electronics nanoTOF II instrument. A Bi_3^{2+} primary ion beam with an ion dose of 5.0 × 10^{11} ions/cm^2 was applied to an area of 100 × 100 μm^2, and negative secondary ions were collected. Charge compensation was performed using 10 eV Ar^+ and 12 eV electrons. The surface sputter cleaning was performed using 20 keV Ar_{2500}^+. The sputtered area was 800 × 800 μm^2 with an ion dose of 5.0 × 10^{14} ions/cm^2. The melamine and highly oriented pyrolytic graphite (HOPG) analytical standards were purchased from Sigma-Aldrich and used without further purification.

First-Principles Calculations. Ab initio molecular dynamics (AIMD) simulations for C_4N_2 were performed within the *NPT* (*N* is the number of particles, *P* the pressure, and *T* the temperature) ensemble[69] implemented in Vienna ab Initio Simulation Package (VASP) code[70] with Langevin dynamics. The all-electron projector-augmented wave (PAW) potential[71] was adopted with the PAW potentials taken from the VASP library where $2s^22p^2$ and $2s^22p^3$ are treated as valence electrons for C and N atoms, respectively. We generated a 2 × 3 × 3 supercell of a conventional unit cell, containing 36 formula units (f.u.) in the simulation cell, which is big enough not to have a force field overlap with the nearest cells. The plane wave was expanded to an energy cutoff of 400 eV, and Brillouin zone sampling with a 1 × 1 × 1 *k*-mesh was employed. Exchange and correlation effects were treated in the Perdew−Burke−Ernzerhof parametrization[72] of the generalized gradient approximation. We also conducted Raman intensity calculations using the Quantum Espresso software package[73] based on density functional perturbation theory.[74] Calculations for vibrational modes need highly accurate charge density, and thus we carefully relaxed the atomic positions and the cell volume at a given external pressure. For the structural relaxation, we used a 6 × 8 × 16 *k*-mesh with 700 eV energy cutoff, and for Raman intensity calculation we used a 4 × 6 × 12 *k*-mesh with 700 eV energy cutoff.

RESULTS AND DISCUSSION

Molecular C_4N_2. C_4N_2 is a centrosymmetric linear molecule.[39] Consequently, it has $3N - 5 = 13$ fundamental vibrational modes, of which the Raman- and IR-active modes can be classified as $\Gamma_{Raman} = 3\Sigma_g^+(\nu_1,\nu_2,\nu_3) + 2\Pi_g(\nu_6,\nu_7)$ and $\Gamma_{IR} = 2\Sigma_u^+(\nu_4,\nu_5) + 2\Pi_u(\nu_8,\nu_9)$, given the molecule's $D_{\infty h}$ symmetry.

DOI: 10.1021/acs.chemmater.7b01446
Chem. Mater. 2017, 29, 6706−6718

Raman and IR spectra of solid C_4N_2 recorded at 0.2 GPa (the solidification pressure at room temperature (RT)) are shown in Figure 1. In order to provide accurate assignments of

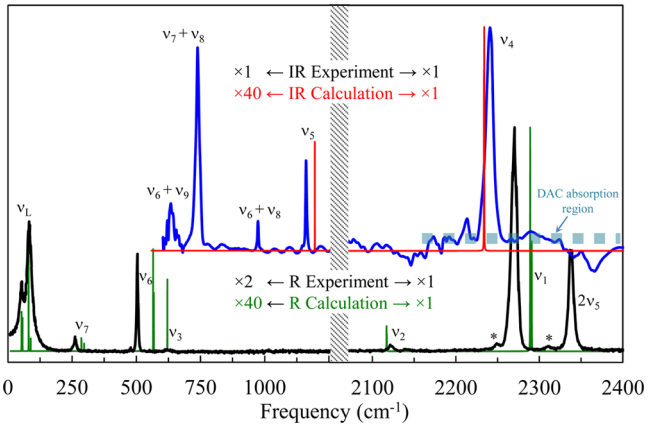

Figure 1. Experimental and calculated Raman (bottom) and IR absorbance (top) spectra of solid C_4N_2 at room temperature (RT) and 0.2 GPa. Calculated spectra are represented by Gaussian peak profiles with an arbitrary width. Spectral intensities are scaled by the factors indicated. Asterisks show contributions from ^{13}C isotopologues. The thick dashed line in the IR spectrum indicates the diamond anvil absorption region.

vibrational modes, we performed density functional perturbation theory calculations, based on the previously reported low-temperature crystal structure (confirmed under pressure, below),[39] to obtain vibrational mode frequencies and intensities. Experimentally, we observed all fundamental modes except the low-frequency IR-active bending modes (ν_8, ν_9), although we are able to infer their experimental frequencies based on observed combination bands. All experimental peak positions exhibit agreement with calculations within a frequency difference of 10%, allowing for accurate assignments.

Significant differences occur between previous mode assignments in the literature, notably in the high-frequency region and the distinction between C≡N and C≡C stretching.[48−54] Our observations indicate that the strongest Raman mode at 2270 cm^{-1} (ν_1) can be assigned to C≡N symmetric stretching, although it is not a pure vibration and shows mixing with C≡C stretching character. The weaker intensity mode at 2122 cm^{-1} (ν_2) is assigned to C≡C stretching. Previously, inconsistent assignments of the C≡N and C≡C stretching modes were made by Miller et al.[48,49] at 2290 and 2119 cm^{-1}, Khanna et al.[50] at 2270 and 2331 cm^{-1}, Smith et al.[51] at 2204 and 2224 cm^{-1}, and Winther et al.[52] at 2268 and 2121 cm^{-1}, together with Bartel et al.[54] at 2296 and 2287 cm^{-1}. Two extremely weak peaks at 2310 and 2138 cm^{-1}, also previously observed at 2309 and 2137 cm^{-1} by Miller et al.,[48,49] and 2307 and 2137 cm^{-1} by Winther et al.,[52] correspond to the naturally abundant ^{13}C isotopologue. The assignments of 618 (ν_3), 505 (ν_6), and 262 (ν_7) cm^{-1} are consistent with previous reports as shown in Table I. Interestingly, two new lattice modes (83 and 51 cm^{-1}) are observed for the first time in our Raman spectrum. The infrared spectrum of C_4N_2 exhibits a strong peak at 2241 cm^{-1} (ν_4), corresponding to asymmetric C≡N and C≡C stretching modes. The observed mode at 1161 cm^{-1} (ν_5) is appropriately assigned to be C−C asymmetric stretching. The strong mode at 2338 cm^{-1} in the Raman spectrum is almost twice the frequency of this mode, which can be assigned to $2\nu_5$.

The in situ behavior of C_4N_2 was also studied under pressure to 13.0 GPa using single-crystal/powder X-ray diffraction. Single-crystal and powder XRD confirm that C_4N_2 crystallizes in the same $P2_1/c$ structure reported previously at low temperature.[35] The lattice parameters obtained at 0.2 GPa of a = 3.878(1) Å, b = 6.058(1) Å, c = 9.0262(2) Å, and β = 98.94(3)° are in good agreement with the low-pressure report (see the SI, Tables S1 and S2 and Figure S1). With increasing pressure, the spectroscopic and diffraction data show that this structure is maintained to 5.5 GPa with a corresponding volume decrease of ∼28% (Figure S2).

Polymerization into an Extended Network. Above 5 GPa, changes in the Raman/IR spectra, as well as distinctive color changes of the sample, indicate the onset of a chemical transformation. The fundamental vibrational modes of C_4N_2 decrease in intensity, while new, broad Raman/IR features (Figure 2b and Figures S3 and S4) are observed near 1200−1600 cm^{-1}. Above 6 GPa the sample transforms from a transparent molecular crystal into a black and visibly opaque solid. Simultaneously, all crystalline diffraction is lost and only a diffuse halo remains visible in X-ray diffraction patterns (Figure 2). These features are indicative of the sp carbon and nitrogen reacting to form a disordered network with largely sp^2 character.

Upon releasing the pressure to ambient conditions, a solid phase with a black luster was recovered, in stark constrast to the transparent starting liquid phase, indicating the irrevesibility of the chemical transformation. The morphology and composition of the recovered phase was examined using SEM with compositional EDS mapping (Figure 3a and Figure S5). The recovered sample exhibits a smooth, uniform texture with homogeneous chemical composition near 30 at.% nitrogen

Table I. Observed and Calculated Raman and IR Modes

		experiment (cm^{-1})	theory (cm^{-1})	assignments
Raman	ν_1 F.r.	2270	2290[a]	symmetricC≡N + C≡C stretching
Raman	ν_2	2122	2117[a]	symmetric C≡C stretching
Raman	ν_3	618	621[a]	Symmetric C−C stretching
IR	ν_4	2241	2234[a]	asymmetric C≡N + C≡C stretching
IR	ν_5	1161	1195[a]	asymmetric C−C stretching
Raman	ν_6	505	565[a]	C−C≡N bending
Raman	ν_7	262	285−296[a]	C≡C−C bending
IR	ν_8	477[b]	509[a]	bending
IR	ν_9	129[b]	120[a]	bending

[a]Most prominent frequency (theory predicts a number of modes of this character due to crystal field splitting). [b]Inferred from combinations. F.r. = Fermi resonance with $2\nu_5$.

DOI: 10.1021/acs.chemmater.7b01446
Chem. Mater. 2017, 29, 6706−6718

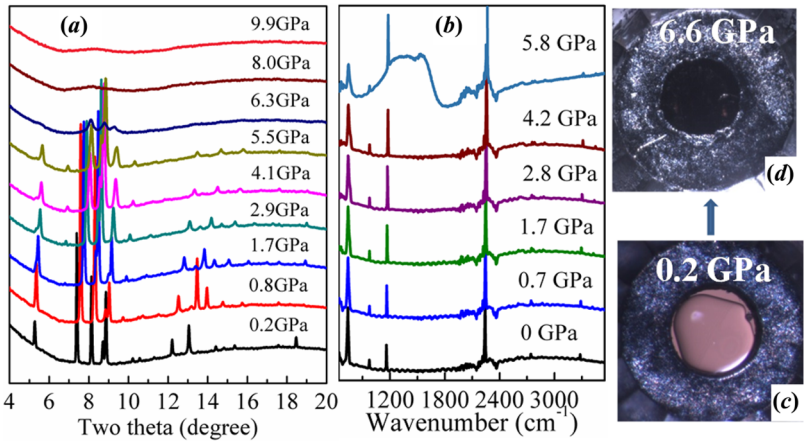

Figure 2. Representative (a) X-ray diffraction patterns, (b) IR spectra, and (c, d) photographs showing the onset of polymerization above ~6 GPa.

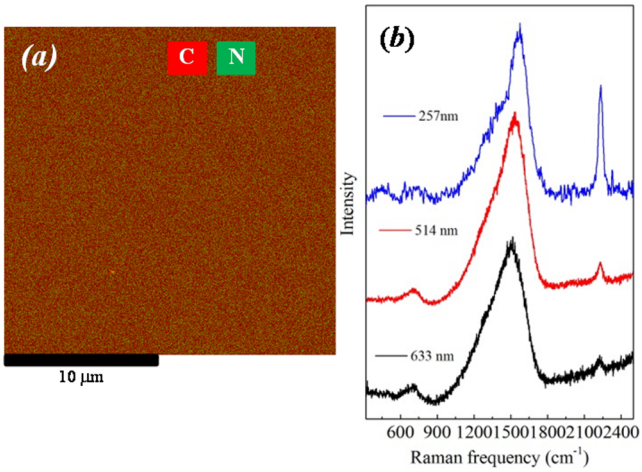

Figure 3. (a) Backscattered electron SEM image showing smooth morphology with overlaid EDS elemental mapping for recovered C_4N_2. The average composition was found to be $C_4N_{1.8\pm0.1}$. (b) Multiwavelength Raman spectra of recovered samples.

($C_4N_{1.8\pm0.1}$). This composition indicates that the majority of nitrogen remains chemically bound within the sample with only a small degree of nitrogen loss, although EDS tends to overestimate carbon content due to various sources of carbon contamination.

Raman spectra from the recovered sample obtained at various laser excitation wavelengths are shown in Figure 3b. The spectra show three notable features, in contrast to the orginial spectra collected from the molecular crystal. A weak peak observed at 2222 (2227) cm^{-1} with 633 (514) nm indicates that a fraction of unconverted sp C≡N and/or C≡C bonding is preserved after the pressure-induced reaction. This sp vibration detected by UV Raman (257 nm) is much stronger than under visible excitation due to resonance enhancement, as also observed in previously amorphous carbon[75−86] and nitride thin film.[87−90] Broad Raman peaks are observed between 900 and 1800 cm^{-1}, as previously observed for amorphous carbons[75−86] or carbon nitrides.[89−98] These "D-" and "G-like" features are associated with C═N and/or C═C sp^2 bonds and indicate the presence of disorder or a range of graphitic domains in the recovered material.[87−90] With increasing excitation wavelengh, these broad peaks shift to lower wavenumber, similar to the G and D bands in amorphous carbon nitrides and carbon materials.[97,98] The peak at 696 cm^{-1} with 633 nm excitation (700 cm^{-1} with 514 nm) is attributed to ring bending modes; this peak is barely visible in the UV Raman results. We note that, due to overlap with the diamond T_{2g} phonon, combined with very weak Raman intensity above 6 GPa, we were not able to study the D and G features using Raman under in situ, high-pressure conditions.

Structure of the Recovered Material. In order to gain deeper insights into the local structure of the recovered C_4N_2, we performed high-energy X-ray scattering experiments to obtain $S(Q)$ to a momentum transfer of Q_{max} = 17 $Å^{-1}$, and transformed this information into the radial distribution function, $g(r)$. In order to help interpret $g(r)$, we performed AIMD simulations at 12 GPa and 300 K and relaxed the reaction product at ambient conditions. We note that a simulation pressure of 12 GPa was required to observe the rare-event chemical reaction on time scales suitable for AIMD simulations. The obtained $g(r)$ for the final disordered C_4N_2 from both experiment and theory are shown in Figure 4a. The $g(r)$ derived from experiment yields an average first-neighbor distance of 1.36 Å, smaller than that of sp^2 amorphous carbon (1.43−1.49 Å) and graphite (1.42 Å).[87,88] The calculated first-neighbor distance is 1.35 Å, which is very close to the experimental result. As suggested from Raman analysis, the recovered sample is dominated by sp^2 C═C and C═N bonds. Compared with known C═C (1.42 Å in graphite and 1.399 Å in benzene) and C═N distances (1.30 Å in furazan, 1.33 Å in pyrazole, 1.34 Å in pyridine, and 1.37 Å in pyrrole),[87] the average first-neighbor distance observed here also confirms that the dominant bonding contributions are from C═C and C═N bonds.

All general features of the experimental $g(r)$ are reproduced by the calculations, suggesting that the calculated structure is a strong candidate to understand the polymeric structure of the disordered product. The structure consists of quasi-two-dimensional layers of sp^2 rings that are sporadically connected by a fraction of sp^3 carbon atoms (<5%) (Figure 4b). This extended polycyclic structure is comprised of mostly five- and six-membered rings, although a small fraction of rings with four and ≥7 members were also observed. The density estimate from the $S(Q)$ and $g(r)$ of the recovered material using the method of Eggert et al.[68] is 2.12 ± 0.1 g/cm^3, compared with 2.17 g/cm^3 from the MD simulation. These values are greater than 2.0 g/cm^3 reported for CN(30%N),[87] but smaller than 2.26 g/cm^3 for crystalline graphite. The calculated average C−C and C−N coordination numbers are 2.4 and 2.9, respectively.

DOI: 10.1021/acs.chemmater.7b01446
Chem. Mater. 2017, 29, 6706−6718

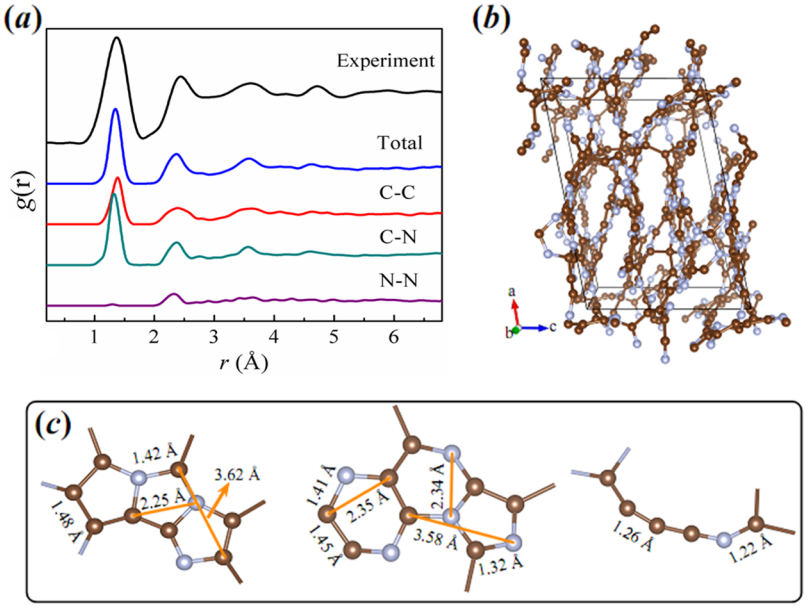

Figure 4. (a) Experimental and calculated $g(r)$ including calculated partial correlations. (b) Relaxed MD structure showing CN network with tendency toward 2D layered structure. (c) Common local motifs with pyridinic- and pyrrolic-like characteristics and a fraction of partially reacted material.

While 5% of the carbon atoms are 4-fold-coordinated, a small fraction of unconverted sp and linear sp^2 carbon keeps the average coordination number below three.

The second-nearest-neighbor peak in $g(r)$ relates to the second coordination shell and thus provides information on bond angles. Experimentally, this peak is located at 2.43 Å, which is slightly longer than 2.37 Å from calculations. These distances provide average bond angles of 124.8° and 122.3° for experiment and calculation, respectively, and indicate a disordered graphitic ring structure. The absence of any distinct features between 2.8 and 3.0 Å indicates that there is no significant fraction of ordered 6-fold rings (the ideal cross-ring, 6-fold peak in graphite occurs at 2.84 Å).[89]

X-ray Photoelectron Spectroscopy. To provide additional information regarding the local structure and bonding features, we performed XPS measurements. The core-level XPS spectrum from the recovered sample is shown in Figure 5. The pristine recovered sample displays both carbon (C 1s) and nitrogen (N 1s) core-level peaks, in addition to a small oxygen contribution, resulting in the approximate chemical composition $C_4N_{1.4}O_{0.24}$. We confirmed that the bulk interior of the sample did not contain any oxygen by performing a soft Ar^+ surface milling to remove ~0.5 Å of material (~20 s at 0.5 kV), after which there was no detectable signal from the O 1s peak above the level of noise (Figure 5a). Thus, the oxygen signal originates from surface oxidation and does not exist within the bulk. After the surface cleaning, the chemical composition of the material indicated partial nitrogen loss ($C_4N_{1.3}$), and we therefore conclude that the chemical composition of the recovered sample falls within the range of $C_4N_{1.4\pm0.1}$ based on XPS analysis, which is in general agreement with the SEM-EDS composition. We note that both XPS (~26% N) and EDS (~31% N) analyses indicate partial nitrogen loss as compared with the starting molecular C_4N_2, but both techniques typically bias carbon due to environmental (adventitious) surface sources, and thus we consider $C_4N_{1.4\pm0.1}$ as a lower bound on the actual nitrogen concentration. Due to the observed nitrogen loss after Ar^+ milling, which suggests possible

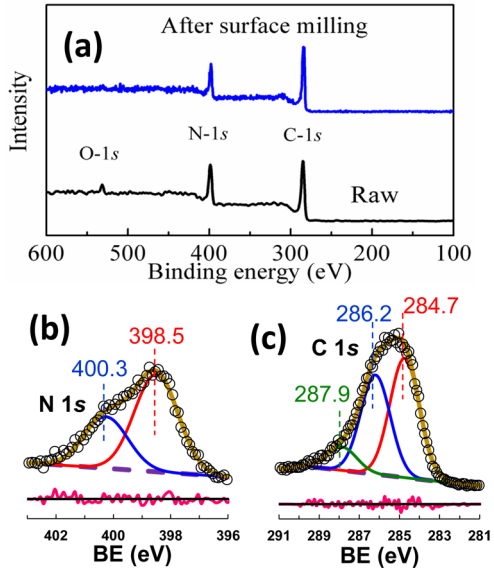

Figure 5. (a) XPS survey for recovered sample before and after ion milling. (b) Representative N 1s and (c) C 1s XPS spectra of the raw surface before ion milling.

alteration of the local chemical structure, we chose to analyze the raw XPS data, before cleaning. We note, however, that there were no major differences between the spectra obtained before and after milling, aside from minor changes in relative peak intensities (and the obvious absence of oxygen).

The carbon nitride literature contains numerous and varying reports concerning the interpretation of XPS spectra.[90−109] XPS spectra provide information regarding the binding energies of core-level electrons, which are a function of the local environment including coordination number and nearest-neighbor constituents. To a first approximation, partial charge, e.g., how much electron density is withdrawn by neighbors, can be used to generalize trends in binding energies. All other factors being equal, an sp^2 carbon bound to another carbon

DOI: 10.1021/acs.chemmater.7b01446
Chem. Mater. 2017, 29, 6706−6718

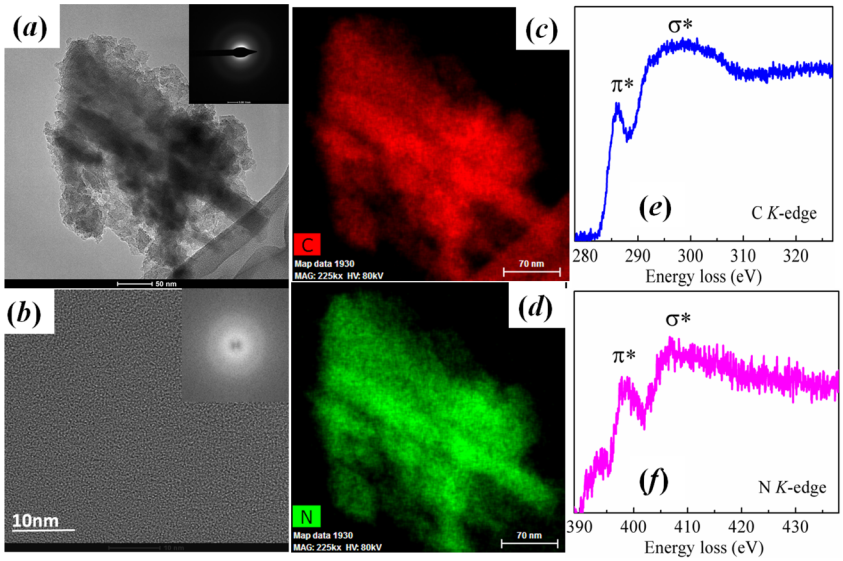

Figure 6. (a) Obtained TEM with diffraction pattern (inset), (b) HRTEM with fast Fourier transformation (inset), elemental analysis of (c) C and (d) N, and EELS of (e) carbon and (f) nitrogen *K*-edges for recovered sample of C_4N_2.

atom will possess a lower binding energy than an sp^2 carbon bound to an oxygen atom. In well-ordered molecular or crystalline systems, it is often straightforward to assign observed binding energies to specific sites, given sufficient spectral resolution. Yet, in disordered materials, such as the recovered C_4N_2 presented here, numerous local environments exist, and spectra should be considered in a statistical manner. Because we do not have sufficient spectral resolution to observe all possible local chemical environments, we employed the following approach to understand the measured XPS spectra. All XPS spectra were processed by first subtracting a linear background function. A series of trial peak functions were tested for each energy region, and it was determined that simple Gaussian peak profiles could sufficiently describe the spectra as well as more-complex functions using the fewest number of adjustable parameters. We used the minimum number of Gaussian peaks needed to adequately fit each spectrum, and each peak within the same binding energy region was constrained to have the same full width at half-maximum (fwhm). Using this approach we can qualitatively understand the prominent local environments present within the recovered samples.

The N 1s core-level region (Figure 5b) was deconvoluted into two different Gaussian components located at 398.5 and 400.3 eV, which are consistent with the general N 1s features reported for amorphous carbon nitride and N-doped graphene.[90−109] The most intense feature at 398.5 eV is attributed to "pyridinic-type" local environments, whereas the less-intense feature at 400.3 eV is attributed to "pyrrolic-type" environments. We note that while this nomenclature is common in the XPS literature, these terms do not explicitly mean pyridine or pyrrole but refer to whether the nitrogen lone pair participates in the π system.[90−112] We were unable to resolve the small contribution from unreacted nitrile groups or any fraction of sp^3 nitrogen atoms. Analysis of structures produced by MD simulations indicates that approximately 46% of the N atoms can be classified as pyridinic (2-fold-coordinated), 29% as pyrrolic (3-fold-coordinated with short C═N bonds), 19% as sp^3 (3-fold-coordinated with long C−N bonds), and 6% as sp. The remaining nitrile nitrogen likely contributes toward the "pyridinic" XPS contribution observed at low binding energy, whereas, the 3-fold-coordinate N atoms with long bonds likely contribute more toward the "pyrrolic" contribution at higher binding energy. Adding these together from calculation, the pyridininc + sp and pyrrolic + sp^3 contributions are roughly 50% each, compared with 69(5)% and 31(5)% averaged over four independent experimental observations. These features are in general agreement, but we note again that it was not possible to precisely describe all expected N 1s chemical environments in the peak fitting.[90,100]

The C 1s core-level spectrum (Figure 5c) is characterized by a broad peak, tailing toward higher binding energy, which is evidence for high sp^2 carbon content in the material.[90−109] The spectrum could be described by three Gaussian components at 284.7, 286.2, and 287.9 eV. The highest BE peak is attributed to C═O bonds on the surface and is expected on the basis of a weak O 1s peak in the survey scan. For sp^2 dominated carbon materials, The XPS literature generally assigns the low BE peak near 284.7 eV to C═C bonds and the higher 286.2 eV peak to C═N bonds.[93,100] But this assignment is incomplete, and the real situation is more complex. Nearly every carbon atom in the recovered material is 3-fold-coordinated; thus the identity of these three neighbors is needed for a base-level interpretation, e.g., CCC, CCN, CNN, and NNN. Our MD simulations reveal no NNN environments, while approximately 39% of three-coordinated carbon atoms are CNN, 52% are CCN, and 9% are CCC. Experimentally, the peaks at 287.7 and 286.2 eV comprise 52(7)% and 48(7)% of the C 1s signal, respectively, when averaged over four independent observations (discounting the contribution of oxygen). Thus, the 284.7 eV peak could represent predominantly CCC and CCN environments, while the 286.2 eV peak could represent CNN environments. While the interpretations across experiment and theory are fully consistent (MD, CCC + CCN = 61% and CNN = 39%; experiment, CCC + CCN = 52(7)% and CNN = 48(7)%), we must emphasize that we cannot fully resolve all C 1s chemical environments. A small fraction of sp^3 carbon and unreacted nitrile carbon will also contribute to the overall shape of the XPS spectrum, although the sp^2 features will dominate.

Transmission Electron Microscopy. High-resolution TEM, together with selected-area electron diffraction (Figure

DOI: 10.1021/acs.chemmater.7b01446
Chem. Mater. 2017, 29, 6706−6718

6), confirms that the material lacks long-range order, in agreement with the X-ray diffraction results. The TEM and EELS measurements were carried out using low beam energy with short acquisition times in order to minimize potential sample damage. HRTEM (Figure 6b) indicates that the material has a smooth texture at the atomic scale and no local domains of order are present. In addition, STEM-EDS mapping (Figure 6c,d) of the recovered sample confirms that carbon and nitrogen are distributed homogeneously with no signs of chemical disproportionation. The full-range EELS spectrum exhibits the characteristic 1s to σ^* and 1s to π^* transitions in both the carbon and nitrogen *K*-edge regions, similar to previous measurements of CN_x films.[102] Zooming in on these regions (Figure 6e,f), the sample shows an abundance of sp^2 bonding in the carbon and nitrogen atoms, as indicated by the presence of 1s peaks at both C and N K-edge. The sp^2 content was calculated to be ~90 ± 5% using graphitized carbon nano-onions as a standard utilizing the method proposed by Brydson et al.[110]

Mass Spectrometry. In order to further study the structure of the disordered carbon nitride, we carried out time-of-flight secondary ion mass spectrometry measurements. The sample surface was cleaned using 20 keV Ar_{2500}^+ ion sputtering to remove signals from surface contaminants and to reveal the true characteristics of the bulk material. The mass spectra of graphitic materials, such as highly oriented pyrolytic graphite (HOPG), do not contain monomeric molecular ions owing to their extended structure. However, graphitic surfaces do exhibit characteristic fragmentation patterns in the negative ion spectrum that consist of a series of prominent C_xH_y peaks with low hydrogen content.[112] The negative ion spectrum of HOPG (as shown in Figure S6) exhibits features associated with C^-, CH^-, C_2^-, C_2H^-, C_3^-, C_4^-, C_5^-, and C_6^-. These prominent features indicate a low hydrogen content and a fragmentation pattern consistent with an extended carbon structure (2D graphite in this case). The negative ion spectrum for recovered C_4N_2 is presented in Figure 7, together with the table of major fragments. In this case, the most prominent fragments are C−N ions (such as CN^-, C_3N^-), C−C ions (such as C^-, C_2^-), and hydrogenated ions with low H content (such as CH^- and C_2H^-). Furthermore, larger C_xN_y fragments with high nitrogen content are also observed. These results confirm the formation of an extended carbon−nitrogen network consisting predominantly of carbon−nitrogen and carbon−carbon bonds and are similar to previously reported results for carbon nitride thin films.[112] In addition, the negative spectrum shows a fragmentation pattern similar to that of the TOF-SIMS spectrum of melamine, but with lower hydrogen content (Figure S7). Compared with the spectrum of melamine, recovered C_4N_2 shows similar low-mass ion fragmentation (e.g., C^-, CH^-, C_2^-, C_2H^-, CN^-, CN_2^-, and $C_2N_3^-$); however, higher mass protonated fragments such as CN_2H^-, $C_2N_3H^-$, and $C_2N_3H_2^-$ are far less prominent.

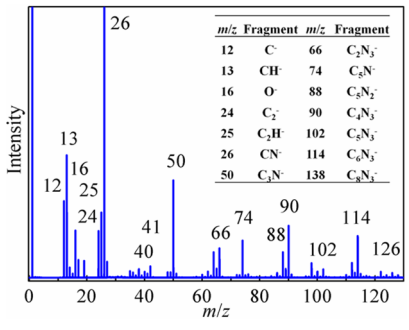

Figure 7. TOF-SIMS negative ion spectrum of the sample after Ar_{2500}^+ ion sputtering. C_xN_y fragments with low content of hydrogen were observed. Although the hydrocarbon contamination on the surface is largely removed by ion sputtering, the contamination is still detected. However, the C_xN_y fragments' peaks are prominent and therefore provide direct evidence of an extended carbon−nitrogen network presented. The negative fragment ions are listed.

Polymerization Mechanism. Previously reported static ab initio calculations suggest that, below 14 GPa, there are no thermodynamically stable crystalline carbon nitride phases[113] including graphitic C_3N_4[114] and its modified allotropes.[115] Here we work in the realm of metastability and examine potential reaction pathways of crystalline, molecular C_4N_2 using a combination of molecular dynamics and metadynamics simulations, as well as evolutionary metadynamics,[116] as implemented in the USPEX code.[117,118] The former is intended to provide direct insights into the reaction mechanism, while the two versions of metadynamics are used to examine a larger portion of the potential energy landscape by overcoming rare-event barriers and to draw conclusions as the system evolves toward the ground state.

Molecular dynamics (*NPT*) trajectories were established from a supercell (36 molecules) of the starting $P2_1/c$ structure at 300 K and 12 GPa. Initial polymerization was generally observed to occur within the first 2 ps of the run (the same polymerized structures were equilibrated at 0 GPa to obtain the $g(r)$ data in Figure 4). The molecular structure can be viewed as two-dimensional sheets of C_4N_2 molecules that lie in a single plane when viewed approximately normal to the (201) direction (Figure 8). Within these sheets, side-aligned columns of C_4N_2 molecules propagate down the *b*-axis. Two types of columns exhibit ABAB stacking within the ~(201) plane where the A column is canted by ~67° with respect to the B column. The shortest interatomic distance in the starting structure is between the nitrile nitrogen of a molecule in column A and the nitrile carbon atom of an adjacent molecule in column B (~3.3 Å at 1 atm).

When compressed to 12 GPa, the linear C_4N_2 molecules began to kink. Some of the C−C≡C and N≡C−C angles drop to as low as 140° within the first 2 ps, indicating enhanced interactions between neighboring molecules. As expected from the starting crystal structure, the initial polymerization initiates between the shortest N···C distance within a single 2D "sheet". The polymerization proceeds within individual sheets through cycloaddition reactions that produce predominantly five- and six-membered rings, giving the overall structure a tendency to propagate in two dimensions. Over time, unreacted bonds begin to form connections between the 2D layers, producing a more interconnected structure that still remains largely two-dimensional. Ultimately, the final disordered C_4N_2 structure is unchanged after ~20 ps. This process is summarized in Figure 9.

At 300 K, MD trajectories become essentially trapped within a single configuration after polymerization occurs—there is not enough energy relative to *kT* for the probable observation of rare-event, covalent-bond breaking at our simulation time scales. In order to gain insights into the tendency of the system to evolve over longer time scales, we performed metadynamics simulations from the starting molecular structure (Figure S8). The metadynamics algorithm uses scaled components of the

DOI: 10.1021/acs.chemmater.7b01446
Chem. Mater. 2017, 29, 6706−6718

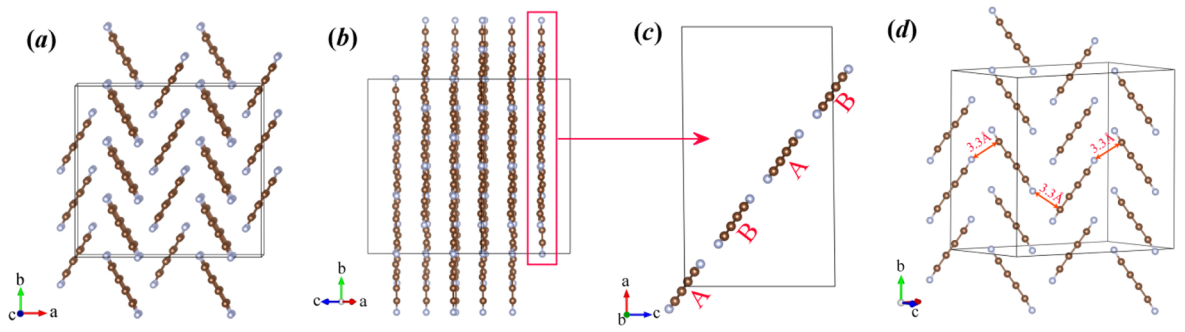

Figure 8. (a) Molecular structure of C_4N_2. (b) View approximately normal to the (201) direction. (c) Molecules forming columns along the *b*-axis with ABAB stacking. (d) Shortest distance between columns, 3.3 Å at 1 atm.

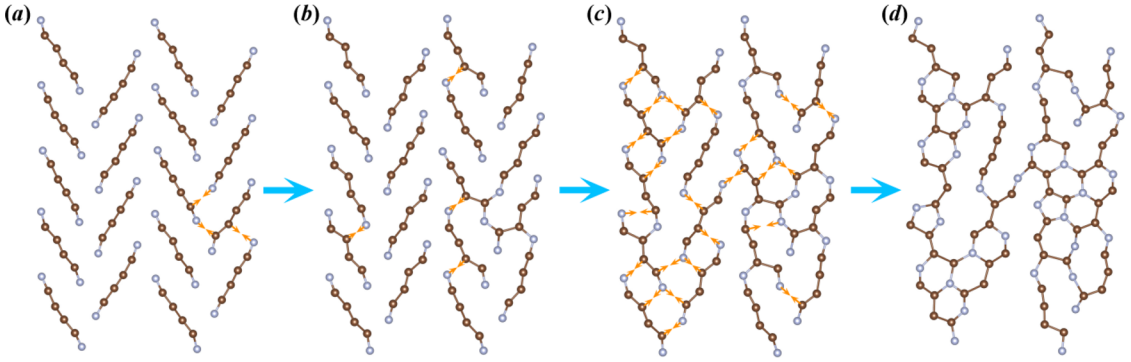

Figure 9. Polymerization process of C_4N_2 at 12 GPa and 300 K shown at (a) 1.8, (b) 2.0, (c) 2.1, and (d) 2.4 ps. Orange arrows indicate reaction points.

edge vectors of the simulation cell as collective variables. The driving force that guides the evolution of the simulation cell is the derivative of the Gibbs free energy with respect to the six collective variables, which were updated in every metastep toward a low-energy pathway to neighboring minima. In our metadynamics simulation, C_4N_2 ultimately transformed to a two-dimensional layered structure. The final layered structure has a very low symmetry with the space group of *P*1, which can be understood as an approximate amorphous structure. The structural evolutions and calculated $g(r)$ for the *P*1 structure and the experimental data are shown in the Supporting Information (Figure S9). The metadynamics reaction sequence and calculated $g(r)$ are very similar when compared with the MD simulations, confirming the mechanism of the reaction process, and the general tendency during the polymerization of C_4N_2 is toward a two-dimensional structure comprised of heterocyclic rings. Interestingly, the evolutionary metadynamics simulations also revealed low-energy 2D and 3D crystalline structures, as reported in the Supporting Information. These structures are reported in Figures S11 and S12 and represent interesting future targets for metastable synthesis.

CONCLUSIONS

In summary, by starting with a hydrogen-free C_4N_2 molecular precursor, an amorphous extended carbon nitride with similar composition can be synthesized via high-pressure, solid-state chemistry. The fundamental vibrational modes of the molecular precursor were also definitively assigned with the help of DFT calculations. The recovered product is a largely two-dimensional polycyclic network comprised of predominantly 3-fold-coordinated sp^2 carbon with "pyrrolic-" and "pyridinic-like" nitrogen. A small fraction of sp^3 carbon connects disordered 2D layers in three dimensions. The reaction proceeds by the activation of linear C_4N_2 molecules into buckled chains that spontaneously assemble through cycloaddition reactions. This understanding of the high-pressure behavior and polymerization mechanism of C_4N_2 will provide fundamental contributions to carbon nitride chemistry.

ASSOCIATED CONTENT

Supporting Information

The Supporting Information is available free of charge on the ACS Publications website at DOI: 10.1021/acs.chemmater.7b01446.

Single-crystal X-ray diffraction analysis, Raman and infrared spectra with pressure, SEM-EDS data, TOF-SIMS data, and metadynamics structures (PDF)

AUTHOR INFORMATION

Corresponding Authors

*(H.G.) E-mail: huiyang.gou@hpstar.ac.cn.
*(T.A.S.) E-mail: tstrobel@ciw.edu.

ORCID

Albert Epshteyn: 0000-0002-4489-2296
Timothy A. Strobel: 0000-0003-0338-4380

Author Contributions

○H.G. and L.Z. contributed equally to this work.

Notes

The authors declare no competing financial interest.
◆NRC Postdoctoral Associate.

DOI: 10.1021/acs.chemmater.7b01446
Chem. Mater. 2017, 29, 6706−6718

■ ACKNOWLEDGMENTS

This work was supported by DARPA under ARO Contract No. W31P4Q-13-I-0005. Portions of this work were performed at HPCAT (Sector 16), Advanced Photon Source (APS), Argonne National Laboratory. HPCAT operations are supported by DOE-NNSA under Award No. DE-NA0001974 and DOE-BES under Award No. DE-FG02-99ER45775, with partial instrumentation funding by NSF. Portions of this work were also carried out at GeoSoilEnviroCARS (The University of Chicago, Sector 13), Advanced Photon Source (APS), Argonne National Laboratory. GeoSoilEnviroCARS is supported by the National Science Foundation—Earth Sciences (Grant EAR-1128799) and Department of Energy—Geo-Sciences (Grant DE-FG02-94ER14466). This research used resources of the Advanced Photon Source, a U.S. Department of Energy (DOE) Office of Science User Facility operated for the DOE Office of Science by Argonne National Laboratory under Contract No. DE-AC02-06CH11357. H.G. acknowledges financial support from the National Natural Science Foundation of China (NSFC) under Grant Nos. 51201148 and U1530402, as well as the Thousand Youth Talents Plan. D.Y.K. acknowledges the Texas Advanced Computing Center (TACC) at the University of Texas at Austin and Argonne Leadership Computing Facility (ALCF), which is a DOE Office of Science User Facility supported under Contract No. DE-AC02-06CH11357, for providing high-performance computing resources.

■ REFERENCES

(1) Liu, A. Y.; Cohen, M. L. Prediction of new low compressibility solids. *Science* **1989**, *245*, 841−842.

(2) Teter, D. M.; Hemley, R. J. Low-compressibility carbon nitrides. *Science* **1996**, *271*, 53−55.

(3) Niu, C.; Lu, Y. Z.; Lieber, C. M. Experimental realization of the covalent solid carbon nitride. *Science* **1993**, *261*, 334−337.

(4) Badding, J. V. Solid-state carbon nitrides. *Adv. Mater.* **1997**, *9*, 877−886.

(5) Thomas, A.; Fischer, A.; Goettmann, F.; Antonietti, M.; Müller, J.-O.; Schlögl, R.; Carlsson, J. M. Graphitic carbon nitride materials: variation of structure and morphology and their use as metal-free catalysts. *J. Mater. Chem.* **2008**, *18*, 4893−4908.

(6) Wang, X.; Maeda, K.; Thomas, A.; Takanabe, K.; Xin, G.; Carlsson, J. M.; Domen, K.; Antonietti, M. A metal-free polymeric photocatalyst for hydrogen production from water under visible light. *Nat. Mater.* **2009**, *8*, 76−80.

(7) Liu, G.; Niu, P.; Sun, C.; Smith, S. C.; Chen, Z.; Lu, G.; Cheng, H. M. Unique electronic structure induced high photoreactivity of sulfur-doped graphitic C_3N_4. *J. Am. Chem. Soc.* **2010**, *132*, 11642−11648.

(8) Wang, Y.; Wang, X.; Antonietti, M. Polymeric graphitic carbon nitride as a heterogeneous organocatalyst: from photochemistry to multipurpose catalysis to sustainable chemistry. *Angew. Chem., Int. Ed.* **2012**, *51*, 68−89.

(9) Zheng, Y.; Liu, J.; Liang, J.; Jaroniec, M.; Qiao, S. Graphitic carbon nitride materials: controllable synthesis and applications in fuel cells and photocatalysis. *Energy Environ. Sci.* **2012**, *5*, 6717−6731.

(10) Li, X. H.; Antonietti, M. Metal nanoparticles at mesoporous N-doped carbons and carbon nitrides: functional Mott-Schottky heterojunctions for catalysis. *Chem. Soc. Rev.* **2013**, *42*, 6593−6604.

(11) Zhu, J.; Xiao, P.; Li, H.; Carabineiro, S. A. C. Graphitic carbon nitride: synthesis, properties, and applications in catalysis. *ACS Appl. Mater. Interfaces* **2014**, *6*, 16449−16465.

(12) Zhao, Z.; Sun, Y.; Dong, F. Graphitic carbon nitride based nanocomposites: a review. *Nanoscale* **2015**, *7*, 15−37.

(13) Cao, S.; Low, J.; Yu, J.; Jaroniec, M. Polymeric photocatalysts based on graphitic carbon nitride. *Adv. Mater.* **2015**, *27*, 2150−2176.

(14) Zheng, Y.; Lin, L.; Wang, B.; Wang, X. Graphitic carbon nitride polymers toward sustainable photoredox catalysis. *Angew. Chem., Int. Ed.* **2015**, *54*, 12868−12884.

(15) Liu, J.; Wang, H.; Antonietti, M. Graphitic carbon nitride "reloaded": emerging applications beyond (photo) catalysis. *Chem. Soc. Rev.* **2016**, *45*, 2308−2326.

(16) Ong, W. J.; Tan, L.; Ng, Y. H.; Yong, S. T.; Chai, S. P. Graphitic carbon nitride (g-C_3N_4)-based photocatalysts for artificial photosynthesis and environmental remediation: are we a step closer to achieving sustainability? *Chem. Rev.* **2016**, *116*, 7159−7329.

(17) Patnaik, S.; Martha, S.; Acharya, S.; Parida, K. M. An overview of the modification of g-C_3N_4 with high carbon containing materials for photocatalytic applications. *Inorg. Chem. Front.* **2016**, *3*, 336−347.

(18) Kang, Y.; Yang, Y.; Yin, L.; Kang, X.; Liu, G.; Cheng, H. Efficient C_3N_4/graphene oxide macroscopic aerogel visible-light photocatalyst. *Adv. Mater.* **2015**, *27*, 4572−4577.

(19) Fan, J.; Chen, J.; Zhang, Q.; Chen, B.; Zang, J.; Zheng, M.; Dong, Q. An Amorphous Carbon Nitride Composite Derived from ZIF-8 as Anode Material for Sodium-Ion Batteries. *ChemSusChem* **2015**, *8*, 1856−1861.

(20) Sjostrom, H.; Hultman, L.; Sundgren, J. E.; Hainsworth, S. V.; Page, T. F.; Theunissen, G. Structural and mechanical properties of carbon nitride CN_x ($0.2 \leqslant x \leqslant 0.35$) films. *J. Vac. Sci. Technol., A* **1996**, *14*, 56−62.

(21) Hellgren, N.; Johansson, M. P.; Broitman, E.; Hultman, L.; Sundgren, J. E. Role of nitrogen in the formation of hard and elastic CN_x thin films by reactive magnetron sputtering. *Phys. Rev. B: Condens. Matter Mater. Phys.* **1999**, *59*, 5162−5169.

(22) Holloway, B. C.; Kraft, O.; Shuh, D. K.; Nix, W. D.; Kelly, M. A.; Pianetta, P.; Hagstrom, S. Interpretation of x-ray photoelectron spectra of elastic amorphous carbon nitride thin films. *Appl. Phys. Lett.* **1999**, *74*, 3290−3292.

(23) Wan, L.; Egerton, R. F. Preparation and characterization of carbon nitride thin films. *Thin Solid Films* **1996**, *279*, 34−42.

(24) Spaeth, C.; Kuhn, M.; Richter, F.; Falke, U.; Hietschold, M.; Kilper, R.; Kreissig, U. A comparative study of elastic recoil detection analysis (ERDA), electron energy loss spectroscopy (EELS) and X-ray photoelectron spectroscopy (XPS) for structural analysis of amorphous carbon nitride films. *Diamond Relat. Mater.* **1998**, *7*, 1727−1733.

(25) Zheng, W. T.; Yu, W. X.; Li, H. B.; Wang, Y. M.; Cao, P. J.; Jin, Z. S.; Broitman, E.; Sundgren, J. E. Chemical bonding, structure, and hardness of carbon nitride thin films. *Diamond Relat. Mater.* **2000**, *9*, 1790−1794.

(26) Gammon, W. D.; Malyarenko, I.; Kraft, O.; Hoatson, G. L.; Reilly, A. C.; Holloway, B. C. Hard and elastic amorphous carbon nitride thin films studied by ^{13}C nuclear magnetic resonance spectroscopy. *Phys. Rev. B: Condens. Matter Mater. Phys.* **2002**, *66*, 153402.

(27) Zhang, Z.; Leinenweber, K.; Bauer, M.; Garvie, L. A. J.; McMillan, P. F.; Wolf, G. H. High-Pressure Bulk Synthesis of Crystalline $C_6N_9H_3$·HCl: A Novel C_3N_4 Graphitic Derivative. *J. Am. Chem. Soc.* **2001**, *123*, 7788−7796.

(28) Jurgens, B.; Irran, E.; Senker, J.; Kroll, P.; Muller, H.; Schnick, W. Melem (2, 5, 8-triamino-tri-s-triazine), an important intermediate during condensation of melamine rings to graphitic carbon nitride: Synthesis, structure determination by X-ray powder diffractometry, solid-state NMR, and theoretical studies. *J. Am. Chem. Soc.* **2003**, *125*, 10288−10300.

(29) Lotsch, B. V.; Schnick, W. Thermal conversion of guanylurea dicyanamide into graphitic carbon nitride via prototype CNx precursors. *Chem. Mater.* **2005**, *17*, 3976−3982.

(30) Lotsch, B. V.; Schnick, W. From Triazines to Heptazines: Novel Nonmetal Tricyanomelaminates as Precursors for Graphitic Carbon Nitride. *Chem. Mater.* **2006**, *18*, 1891−1900.

(31) Horvath-Bordon, E.; Riedel, R.; McMillan, P. F.; Kroll, P.; Miehe, G.; van Aken, P. A.; Zerr, A.; Hoppe, P.; Shebanova, O.; Mclaren, I.; Lauterbach, S.; Kroke, E.; Boehler, R. High-Pressure

DOI: 10.1021/acs.chemmater.7b01446
Chem. Mater. 2017, 29, 6706−6718

Synthesis of Crystalline Carbon Nitride Imide, $C_2N_2(NH)$. *Angew. Chem., Int. Ed.* **2007**, *46*, 1476−1480.
(32) Salamat, A.; Deifallah, M.; Cabrera, R. Q.; Cora, R.; McMillan, P. F. Identification of new pillared-layered carbon nitride materials at high pressure. *Sci. Rep.* **2013**, *3*, 2122.
(33) Schettino, V.; Bini, R. Molecules under extreme conditions: Chemical reactions at high pressure. *Phys. Chem. Chem. Phys.* **2003**, *5*, 1951−1965.
(34) Yoo, C. S.; Nicol, M. F. Chemical and phase transformations of cyanogen at high pressures. *J. Phys. Chem.* **1986**, *90*, 6726−6731.
(35) Aoki, K.; Kakudate, Y.; Yoshida, M.; Usuba, S.; Fujiwara, S. Solid state polymerization of cyanoacetylene into conjugated linear chains under pressure. *J. Chem. Phys.* **1989**, *91*, 778−782.
(36) Tomasino, D.; Chen, J.-Y.; Kim, M.; Yoo, C.-S. Pressure-induced phase transition and polymerization of tetracyanoethylene (TCNE). *J. Chem. Phys.* **2013**, *138*, 094506.
(37) Gou, H.; Yonke, B. L.; Epshteyn, A.; Kim, D. Y.; Smith, J. S.; Strobel, T. A. Pressure-induced polymerization of $P(CN)_3$. *J. Chem. Phys.* **2015**, *142*, 194503.
(38) Zheng, H.; Li, K.; Cody, G.; Tulk, C. A.; Dong, X.; Gao, G.; Molaison, J. J.; Liu, Z.; Feygenson, M.; Yang, W.; Ivanov, I. N.; Basile, L.; Idrobo, J.-C.; Guthrie, M.; Mao, H. Polymerization of Acetonitrile via a Hydrogen Transfer Reaction from CH_3 to CN under Extreme Conditions. *Angew. Chem., Int. Ed.* **2016**, *55*, 12040−12044.
(39) Hannan, R. B.; Collin, R. L. The crystal structure of dicyanoacetylene. *Acta Crystallogr.* **1953**, *6*, 350−352.
(40) Armstrong, G. T.; Marantz, S. The Heat of Combustion of Dicyanoacetylene. *J. Phys. Chem.* **1963**, *67*, 2888.
(41) Kirshenbaum, A. D.; Grosse, A. V. The combustion of carbon subnitride, C4N2, and a chemical method for the production of continuous tempertures in the range of 5000−6000° K. *J. Am. Chem. Soc.* **1956**, *78*, 2020.
(42) Ciganek, E. Diels-Alder additions of dicyanoacetylene to aromatic hydrocarbons. *Tetrahedron Lett.* **1967**, *8*, 3321−3325.
(43) Chien, J. C. W.; Carlini, C. Semiconducting poly-(dicyanoacetylenes). *J. Polym. Sci., Polym. Chem. Ed.* **1985**, *23*, 1383−1393.
(44) Coll, P.; Guillemin, J.-C.; Gazeau, M.-C.; Raulin, F. Report and implications of the first observation of C_4N_2 in laboratory simulations of Titan's atmosphere. *Planet. Space Sci.* **1999**, *47*, 1433−1440.
(45) Nishio, M.; Paillous, P.; Khlifi, M.; Bruston, P.; Raulin, F. Infrared spectra of gaseous ethanenitrile in the 3500−250 cm^{-1} region: absolute band intensity and implications for the atmosphere of Titan. *Spectrochim. Acta, Part A* **1995**, *51*, 617−622.
(46) Samuelson, R. E.; Mayo, L. A.; Knuckles, M. A.; Khanna, R. J. C_4N_2 ice in Titan's north polar stratosphere. *Planet. Space Sci.* **1997**, *45*, 941−948.
(47) de Kok, R. J.; Teanby, N. A.; Maltagliati, L.; Irwin, P. G. J.; Vinatier, S. HCN ice in Titan's high-altitude southern polar cloud. *Nature* **2014**, *514*, 65−67.
(48) Miller, F. A.; Hannan, R. B., Jr. The Infrared and Raman Spectra of Dicyanoacetylene. *J. Chem. Phys.* **1953**, *21*, 110−114.
(49) Miller, F. A.; Hannan, R. B., Jr.; Cousins, L. R. Infrared and Raman Spectra of Dicyanoacetylene. II. *J. Chem. Phys.* **1955**, *23*, 2127−2129.
(50) Khanna, R. K.; Perera-Jarmer, M. A.; Ospina, M. J. Vibrational infrared and Raman spectra of dicyanoacetylene. *Spectrochim. Acta, Part A* **1987**, *43*, 421−425.
(51) Smith, A. M.; Schallmoser, G.; Thoma, A.; Bondybey, V. E. Infrared spectral evidence of N≡C-C≡C-N≡C:Photoisomerization of N≡C-C≡C-N≡C in an argon matrix. *J. Chem. Phys.* **1993**, *98*, 1776−1785.
(52) Winther, F.; Schonhoff, M. The Fundamental Vibrations of N≡C-C≡C-N≡C (Dicyanoacetylene). *J. Mol. Spectrosc.* **1997**, *186*, 54−65.
(53) Khlifi, M.; Paillous, P.; Bruston, P.; Guillemin, J. C.; Benilan, Y.; Daoudi, A.; Raulin, F. Gas infrared spectra, assignments, and absolute IR band intensities of C_4N_2 in the 250−3500 cm^{-1} region: implications for Titan's stratosphere. *Spectrochim. Acta, Part A* **1997**, *53*, 707−712.
(54) Bartel, C.; Botschwina, P.; Bürger, H.; Guarnieri, A.; Heyl, A.; Huckauf, A.; Lentz, D.; Merzliak, T.; Mkadmi, E. B. Cyanoisocyanoacetylene, N≡C-C≡C-N≡C. *Angew. Chem., Int. Ed.* **1998**, *37*, 2879−2882.
(55) Saggiomo, A. J. The Dinitriles of Acetylenedicarboxylic and Polyacetylenedicarboxylic Acids. 1 I. 2 Dicyanoacetylene and Dicyanodiacetylene. *J. Org. Chem.* **1957**, *22*, 1171−1175.
(56) Mao, H. K.; Xu, J.; Bell, P. M. Calibration of the ruby pressure gauge to 800 kbar under quasi-hydrostatic conditions. *J. Geophys. Res.* **1986**, *91*, 4673−4676.
(57) Hammersley, A. P.; Svensson, S. O.; Hanfland, M.; Fitch, A. N.; Häusermann, D. Two-dimensional detector software: from real detector to idealized image or two-theta scan. *High Pressure Res.* **1996**, *14*, 235−248.
(58) Le Bail, A. ESPOIR: a program for solving structures by Monte Carlo from powder diffraction data. *Mater. Sci. Forum* **2001**, *378*−*381*, 65−70.
(59) Larson, A. C.; Von Dreele, R. B. *General Structure Analysis System (GSAS)*, Report LAUR 86-748; Los Alamos National Laboratory: Los Alamos, NM, USA, 2000.
(60) Desgreniers, S.; Lagarec, K. XRDA3.1-a program for X-ray diffraction analysis on a PC. *J. Appl. Crystallogr.* **1998**, *31*, 109−110.
(61) Dera, P.; Zhuravlev, K.; Prakapenka, V.; Rivers, M. L.; Finkelstein, G. J.; Grubor-Urosevic, O.; Tschauner, O.; Clark, S. M.; Downs, R. T. High pressure single-crystal micro X-ray diffraction analysis with GSE_ADA/RSV software. *High Pressure Res.* **2013**, *33* (3), 466−484.
(62) Sheldrick, G. A short history of SHELX. *Acta Crystallogr., Sect. A: Found. Crystallogr.* **2008**, *64* (1), 112−122.
(63) Sheldrick, G. Crystal structure refinement with SHELXL. *Acta Crystallogr., Sect. C: Struct. Chem.* **2015**, *71* (1), 3−8.
(64) Parthe, E.; Gelato, L. M. The standardization of inorganic crystal-structure data. *Acta Crystallogr., Sect. A: Found. Crystallogr.* **1984**, *40* (3), 169−183.
(65) Gelato, L. M.; Parthe, E. STRUCTURE TIDY−a computer program to standardize crystal structure data. *J. Appl. Crystallogr.* **1987**, *20* (2), 139−143.
(66) Prescher, C.; Prakapenka, V. B. DIOPTAS: a program for reduction of two-dimensional X-ray diffraction data and data exploration. *High Pressure Res.* **2015**, *35*, 223−230.
(67) Eggert, J.; Weck, G.; Loubeyre, P.; Mezouar, M. Quantitative structure factor and density measurements of high-pressure fluids in diamond anvil cells by x-ray diffraction: Argon and water. *Phys. Rev. B: Condens. Matter Mater. Phys.* **2002**, *65*, 174105.
(68) Kaplow, R.; Strong, S. L.; Averbach, B. L. Radial density functions for liquid mercury and lead. *Phys. Rev.* **1965**, *138*, A1336−1345.
(69) Hernández, E. Metric-tensor flexible-cell algorithm for isothermal−isobaric molecular dynamics simulations. *J. Chem. Phys.* **2001**, *115*, 10282−10290.
(70) Kresse, G.; Furthmüller, J. Efficient iterative schemes for ab initio total-energy calculations using a plane-wave basis set. *Phys. Rev. B: Condens. Matter Mater. Phys.* **1996**, *54*, 11169−11186.
(71) Kresse, G.; Joubert, D. From ultrasoft pseudopotentials to the projector augmented-wave method. *Phys. Rev. B: Condens. Matter Mater. Phys.* **1999**, *59*, 1758−1775.
(72) Perdew, J. P.; Burke, K.; Ernzerhof, M. Generalized gradient approximation made simple. *Phys. Rev. Lett.* **1996**, *77*, 3865−3868.
(73) Giannozzi, P.; Baroni, S.; Bonini, N.; et al. QUANTUM ESPRESSO: a modular and open-source software project for quantum simulations of materials. *J. Phys.: Condens. Matter* **2009**, *21*, 395502.
(74) Baroni, S.; de Gironcoli, S.; Dal Corso, A.; Giannozzi, P. Phonons and related crystal properties from density-functional perturbation theory. *Rev. Mod. Phys.* **2001**, *73*, 515−562.
(75) Ferrari, A. C.; Robertson, J. Origin of the 1150 cm^{-1} Raman mode in nanocrystalline diamond. *Phys. Rev. B: Condens. Matter Mater. Phys.* **2001**, *63*, 121405.

DOI: 10.1021/acs.chemmater.7b01446
Chem. Mater. 2017, 29, 6706−6718

(76) Ferrari, A. C.; Rodil, S. E.; Robertson, J. Interpretation of infrared and Raman spectra of amorphous carbon nitrides. *Phys. Rev. B: Condens. Matter Mater. Phys.* **2003**, *67*, 155306.
(77) Ferrari, A. C.; Rodil, S. E.; Robertson, J. Resonant Raman spectra of amorphous carbon nitrides: the G peak dispersion. *Diamond Relat. Mater.* **2003**, *12*, 905−910.
(78) Ferrari, A. C.; Robertson, J. Raman spectroscopy of amorphous, nanostructured, diamond−like carbon, and nanodiamond. *Philos. Trans. R. Soc., A* **2004**, *362*, 2477−2512.
(79) Rodil, S. E.; Muhl, S. Bonding in amorphous carbon nitride. *Diamond Relat. Mater.* **2004**, *13*, 1521−1531.
(80) Tamor, M. A.; Wu, C. H. Graphitic network models of "diamondlike" carbon. *J. Appl. Phys.* **1990**, *67*, 1007−1012.
(81) Kaufman, J. H.; Metin, S.; Saperstein, D. D. Symmetry breaking in nitrogen-doped amorphous carbon: Infrared observation of the Raman-active G and D bands. *Phys. Rev. B: Condens. Matter Mater. Phys.* **1989**, *39*, 13053−13060.
(82) Beeman, D.; Silverman, J.; Lynds, R.; Anderson, M. R. Modeling studies of amorphous carbon. *Phys. Rev. B: Condens. Matter Mater. Phys.* **1984**, *30*, 870−875.
(83) Shi, J. R.; Shi, X.; Sun, Z.; Liu, E.; Tay, B. K.; Lau, S. P. Ultraviolet and visible Raman studies of nitrogenated tetrahedral amorphous carbon films. *Thin Solid Films* **2000**, *366*, 169−174.
(84) Ferrari, A. C.; Robertson, J. Interpretation of Raman spectra of disordered and amorphous carbon. *Phys. Rev. B: Condens. Matter Mater. Phys.* **2000**, *61*, 14095−14107.
(85) Ferrari, A. C.; Robertson, J. Resonant Raman spectroscopy of disordered, amorphous, and diamondlike carbon. *Phys. Rev. B: Condens. Matter Mater. Phys.* **2001**, *64*, 075414.
(86) Casari, C. S.; Li Bassi, A.; Baserga, A.; Ravagnan, L.; Piseri, P.; Lenardi, C.; Tommasini, M.; Milani, A.; Fazzi, D.; Bottani, C. E.; Milani, P. Low-frequency modes in the Raman spectrum of *sp*− sp^2 nanostructured carbon. *Phys. Rev. B: Condens. Matter Mater. Phys.* **2008**, *77*, 195444.
(87) Walters, J. K.; Kühn, M.; Spaeth, C.; Fischer, H.; Richter, F.; Newport, R. J. Neutron-diffraction studies of amorphous CN_x materials. *Phys. Rev. B: Condens. Matter Mater. Phys.* **1997**, *56*, 14315−14320.
(88) Clark, S. J.; Crain, J.; Ackland, G. J. Comparison of bonding in amorphous silicon and carbon. *Phys. Rev. B: Condens. Matter Mater. Phys.* **1997**, *55*, 14059−14062.
(89) Li, F.; Lannin, J. S. Radial distribution function of amorphous carbon. *Phys. Rev. Lett.* **1990**, *65*, 1905−1908.
(90) Titantah, J. T.; Lamoen, D. Carbon and nitrogen 1s energy levels in amorphous carbon nitride systems: XPS interpretation using first-principles. *Diamond Relat. Mater.* **2007**, *16*, 581−588.
(91) Bartle, K. D.; Perry, D. L.; Wallace, S. The functionality of nitrogen in coal and derived liquids: an XPS study. *Fuel Process. Technol.* **1987**, *15*, 351−361.
(92) Kelemen, S. R.; Gorbaty, M. L.; Kwiatek, P. J. Quantification of nitrogen forms in Argonne premium coals. *Energy Fuels* **1994**, *8*, 896−906.
(93) Hellgren, N.; Haasch, R. T.; Schmidt, S.; Hultman, L.; Petrov, I. Interpretation of X-ray photoelectron spectra of carbon-nitride thin films: New insights from in situ XPS. *Carbon* **2016**, *108*, 242−252.
(94) D'Anna, E.; De Giorgi, M. L.; Luches, A.; Martino, M.; Perrone, A.; Zocco, A. Study of C-N binding states in carbon nitride films deposited by reactive XeCl laser ablation. *Thin Solid Films* **1999**, *347*, 72−77.
(95) Ech-chamikh, E.; Essafti, A.; Ijdiyaou, Y.; Azizan, M. XPS study of amorphous carbon nitride (aC:N) thin films deposited by reactive RF sputtering. *Sol. Energy Mater. Sol. Cells* **2006**, *90*, 1420−1423.
(96) Pels, J. R.; Kapteijn, F.; Moulijn, J. A.; Zhu, Q.; Thomas, K. M. Evolution of nitrogen functionalities in carbonaceous materials during pyrolysis. *Carbon* **1995**, *33*, 1641−1653.
(97) Estrade-Szwarckopf, H. XPS photoemission in carbonaceous materials: A "defect" peak beside the graphitic asymmetric peak. *Carbon* **2004**, *42*, 1713−1721.
(98) Zheng, W. T.; Xing, K. Z.; Hellgren, N.; Lögdlund, M.; Johansson, Å.; Gelivs, U.; Salaneck, W. R.; Sundgren, J.-E. Nitrogen 1s electron binding energy assignment in carbon nitride thin films with different structures. *J. Electron Spectrosc. Relat. Phenom.* **1997**, *87*, 45−49.
(99) Hellgren, N.; Johansson, M. P.; Broitman, E.; Hultman, L.; Sundgren, J. E. Role of nitrogen in the formation of hard and elastic CN_x thin films by reactive magnetron sputtering. *Phys. Rev. B: Condens. Matter Mater. Phys.* **1999**, *59*, 5162−5169.
(100) Ronning, C.; Feldermann, H.; Merk, R.; Hofsass, H.; Reinke, P.; Thiele, J. U. Carbon nitride deposited using energetic species: a review on XPS studies. *Phys. Rev. B: Condens. Matter Mater. Phys.* **1998**, *58*, 2207−2215.
(101) Ripalda, J. M.; Román, E.; Díaz, N.; Galán, L.; Montero, I.; Comelli, G.; Baraldi, A.; Lizzit, S.; Goldoni, A.; Paolucci, G. Correlation of X-ray absorption and X-ray photoemission spectroscopies in amorphous carbon nitride. *Phys. Rev. B: Condens. Matter Mater. Phys.* **1999**, *60*, R3705−R3708.
(102) Braun, A.; Huggins, F. E.; Shah, N.; Chen, Y.; Wirick, S.; Mun, S. B.; Jacobsen, C.; Huffman, G. P. Advantages of soft X-ray absorption over TEM-EELS for solid carbon studies−−a comparative study on diesel soot with EELS and NEXAFS. *Carbon* **2005**, *43*, 117−124.
(103) Qu, L.; Liu, Y.; Baek, J.; Dai, L. Nitrogen-doped graphene as efficient metal-free electrocatalyst for oxygen reduction in fuel cells. *ACS Nano* **2010**, *4*, 1321−1321.
(104) Geng, D.; Chen, Y.; Chen, Y.; Li, Y.; Li, R.; Sun, X.; Ye, S.; Knights, S. High oxygen-reduction activity and durability of nitrogen-doped grapheme. *Energy Environ. Sci.* **2011**, *4*, 760−764.
(105) Wang, H.; Maiyalagan, T.; Wang, X. Review on recent progress in nitrogen-doped graphene: synthesis, characterization, and its potential applications. *ACS Catal.* **2012**, *2*, 781−794.
(106) Warner, J. H.; Lin, H. C.; He, K.; Koshino, M.; Suenaga, K. Stability and spectroscopy of single nitrogen dopants in graphene at elevated temperatures. *ACS Nano* **2014**, *8*, 11806−11815.
(107) Arenal, R.; March, K.; Ewels, C. P.; Rocquefelte, X.; Kociak, M.; Loiseau, A.; Stephan, O. Atomic configuration of nitrogen-doped single-walled carbon nanotubes. *Nano Lett.* **2014**, *14*, 5509−5516.
(108) Lin, Y.; Teng, P.; Yeh, C.; Koshino, M.; Chiu, P.; Suenaga, K. Structural and chemical dynamics of pyridinic-nitrogen defects in grapheme. *Nano Lett.* **2015**, *15*, 7408−7413.
(109) Gupta, N. K.; Peng, B.; Haller, G. L.; Ember, E. E.; Lercher, J. A. Nitrogen Modified Carbon Nano-Materials as Stable Catalysts for Phosgene Synthesis. *ACS Catal.* **2016**, *6*, 5843−5855.
(110) Brydson, R.; Zhili, Z.; Brown, A. Revisiting the determination of carbon sp^2/sp^3 ratios via analysis of the EELS carbon K-edge. *Vol. 1: Instrumentation and Methods* **2008**, *12*, 357−358.
(111) Deslandes, A.; Jasieniak, M.; Ionescu, M.; Shapter, J. G.; Fairman, C.; Gooding, J. J.; Hibbert, D. B.; Quinton, J. S. ToF-SIMS characterisation of methane- and hydrogen-plasma-modified graphite using principal component analysis. *Surf. Interface Anal.* **2009**, *41*, 216−224.
(112) Huang, L. J.; Hung, Y.; Chang, S.; Massoumi, G. R.; Lennard, W. N.; Mitchell, I. V. Characterization of carbon and carbon nitride thin films using time-of-flight secondary-ion-mass spectrometry. *J. Vac. Sci. Technol., A* **1997**, *15*, 2196−2201.
(113) Dong, H.; Oganov, A. R.; Zhu, Q.; Qian, G. The phase diagram and hardness of carbon nitrides. *Sci. Rep.* **2015**, *5*, 9870.
(114) Kroke, E. gt-C_3N_4-The First Stable Binary Carbon (IV) Nitride. *Angew. Chem., Int. Ed.* **2014**, *53*, 11134−11135.
(115) Pickard, C. J.; Salamat, A.; Bojdys, M. J.; Needs, R. J.; McMillan, P. F. Carbon nitride frameworks and dense crystalline polymorphs. *Phys. Rev. B: Condens. Matter Mater. Phys.* **2016**, *94*, 094104.
(116) Zhu, Q.; Oganov, A. R.; Lyakhov, A. O. Evolutionary metadynamics: a novel method to predict crystal structures. *CrystEngComm* **2012**, *14*, 3596−3601.
(117) Oganov, A. R.; Glass, C. W. Crystal structure prediction using ab initio evolutionary techniques: Principles and applications. *J. Chem. Phys.* **2006**, *124*, 244704.

DOI: 10.1021/acs.chemmater.7b01446
Chem. Mater. 2017, 29, 6706−6718

(118) Lyakhov, A. O.; Oganov, A. R.; Stokes, H. T.; Zhu, Q. New developments in evolutionary structure prediction algorithm USPEX. *Comput. Phys. Commun.* **2013**, *184*, 1172−1182.

DOI: 10.1021/acs.chemmater.7b01446
Chem. Mater. 2017, 29, 6706−6718